Unresolved stress tensor modeling in turbulent premixed V-flames using iterative deconvolution: An *a priori* assessment

Z. M. Nikolaou[*]
Computation-Based Science and Technology Research Centre (CaSToRC), The Cyprus Institute, Nicosia 2121, Cyprus

Y. Minamoto[†]
Department of Mechanical Engineering, Tokyo Institute of Technology, 2-12-1 Ookayama, Meguro-ku, Tokyo 152-8550, Japan

L. Vervisch[‡]
CORIA–CNRS, Normandie Université, INSA de Rouen Normandie, France

(Received 20 February 2019; published 11 June 2019)

The unresolved stress tensor in large-eddy simulations is an important unclosed term which affects the evolution of the resolved kinetic energy and consequently the evolution of large-scale motions. The literature on modeling this term for nonreacting flows is substantial but very scarce for turbulent flames and reacting flows with nonuniform density in general. The modeling assumptions in classic models are often strong even for nonreacting flows, which limits their range of applicability. In this study, a method using an iterative reconstruction algorithm is used in order to model the unresolved stress tensor for a highly demanding flow configuration which involves reaction, modeled using detailed chemistry, and mean shear. The evaluation of the method is conducted *a priori* using direct numerical simulation data, which are filtered and then sampled onto a coarser mesh. The performance of the method is compared against eight different classic models in the literature which include both static and dynamic formulations.

DOI: 10.1103/PhysRevFluids.4.063202

I. INTRODUCTION

A large amount of literature has been devoted to the subject of modeling the unresolved stress tensor in large-eddy simulations (LES), with the majority of models developed and evaluated for nonreacting and incompressible flows. In reacting flows, the usual practice is to assume that such models are also applicable despite the fundamentally different flow physics. Heat release, for example, causes a local expansion of the flow field and large changes in viscosity, both of which directly affect the turbulence dissipation/backscatter characteristics. In a recent study, and one of the few of its kind, several such classic models (originally developed for nonreacting flows) were tested *a priori* for reacting flows, using direct numerical simulation (DNS) data of turbulent premixed freely propagating flames [1]. Significant differences were observed between the models' predictions, while the correlation coefficients for some of the most popular models were in the

[*]z.nicolaou@cyi.ac.cy
[†]minamoto.y.aa@m.titech.ac.jp
[‡]vervisch@coria.fr

region of 0.2–0.4 only. Clearly, heat release effects should be accounted for, and to achieve that the model essentially needs to be by construction insensitive to the flow physics. Furthermore, more work on modeling this important term is required for reacting flows. The objectives of this study are to address these two issues by proposing a modeling approach for the unresolved stress tensor using deconvolution, and by examining *a priori* the performance of several models for the unresolved stresses for a highly demanding turbulent and reacting flow which also involves mean shear, using DNS data of a rod-stabilized V-flame.

The Smagorinsky model was amongst the models tested in [1]. Originally developed for atmospheric flows [2], it is one of the most popular models to date which has been employed in many LES studies. It is an eddy-diffusivity type of model, relatively straightforward to implement, and computationally efficient. However, from a theoretical point of view there are some important issues. The primary issue is that it is a purely dissipative model, whereas a reverse flow of energy is known to exist from the small scales to the large scales in two-dimensional flows as shown by Fjortoft [3], and similar situations are encountered in three-dimensional flows [4–6]. In addition, the assumption of the unresolved stress tensor, τ_{ij}, being aligned to the resolved rate of strain tensor, $\tilde{S}_{ij}$, is a rather strong one as shown by previous experimental and numerical studies [7,8]. Another issue, is that the model predictions are sensitive to the value of the model parameter C_S (Smagorinsky constant) which depends on the flow regime [9,10], but also on the filter width and mesh spacing [11]. These limitations soon became apparent, which led to the development of a dynamic version by Germano [12]. The dynamic Smagorinsky model showed considerable improvement over its static version, particularly in shear flows [12], and was later adapted to compressible flows by Moin *et al.* [13]. It is important to note, however, that a regularization procedure is often required for the evaluation of dynamic parameters in order to render them spatially smooth, thus avoiding numerical instabilities. This process is not always unique or justifiable, and typically involves averaging in homogeneous directions (if any), thresholding, smoothing, or otherwise if no homogeneous directions exist such as Lagrangian averaging [14]. Consequently, an ensemble of submodels actually exist depending on the regularization process used. Overall, care has to be taken so that the regularization process does not result in large spatiotemporal variations of the dynamic parameters [15].

Gradient-type models are an attractive alternative [16,17]. Vreman *et al.* [18] showed that such models can be obtained by a Taylor series expansion of the stress tensor, and retaining the leading term in the expansion. Such models do not involve any tunable parameters, and in principle their accuracy can be improved by including additional terms in the expansion. In the same study [18], the performance of a number of different models was evaluated both *a priori* and *a posteriori*, using LES of a temporal mixing layer. It was shown, however, that models of the gradient type, including only the leading term in the Taylor series expansion, did not provide sufficient dissipation. Incorporating an eddy-diffusivity component, on the other hand (mixed model), caused excessive dissipation. A dynamic and mixed model was therefore proposed which showed the best performance [18].

Another class of models termed scale similarity, were proposed by Bardina [19]. Scale-similarity models can be shown to reduce to a gradient-type model by expanding in Taylor series the filtered velocity product in the expression for the unresolved stress tensor, $\tau_{ij} = \bar{\rho}(\widetilde{u_i u_j} - \tilde{u}_i \tilde{u}_j)$ [18]. Scale-similarity models, however, were also found to provide insufficient dissipation in *a posteriori* studies, and mixed models were employed for stable simulations combining a scale-similarity basis with an eddy-diffusivity component [19]. In [20], a thorough *a posteriori* assessment of six different models using LES of a turbulent mixing layer was conducted. The models tested included Smagorinsky, scale-similarity, gradient, dynamic Smagorinsky, dynamic mixed (similarity+eddy-diffusivity), and a dynamic Clark model (gradient+eddy-diffusivity) [17]. In general, the dynamic models had a substantially improved performance compared to the static models, with the mixed models having the best overall agreement. Closures of the mixed kind have generally been very successful, and were used in many later studies as a prototype for developing improved models such as the wall-adapting local-eddy viscosity (WALE) model [21]. A multitude of different models have in fact been developed in the literature, focusing on nonreacting flows, and a thorough review is given by Meneveau and Katz [22].

In reacting and compressible flows, six different models for the unresolved stress tensor were tested *a priori* in [1]. Of all the models tested, both the static and dynamic versions of the Smagorinsky model had the poorest correlation coefficients; the Smagorinsky model relies on the Boussinesq assumption, which may not be the best approximation for variable density flows featuring very localized heat release rates. This fact was also demonstrated experimentally by Pfandler *et al.* [23], where the density-weighted stress tensor was directly measured. Furthermore, it was shown in [1] that the standard averaging procedure for regularizing the dynamic Smagorinsky parameter was inadequate. The rest of the models showed significantly larger correlation coefficients; however, it is important to note that the database used in [1] did not involve mean shear, and the assessment was conducted on the fine DNS mesh. Hence, it is unclear how the models will perform for shear and reacting flows on a coarser mesh. In any case, the modeling should be able to account for the effects of heat release. These important points were indicated in many previous theoretical and experimental studies [1,23–25]. At the same time, a model needs to be simple and straightforward to implement. This implies that the functional relationship between the unresolved stresses and the resolved LES variables needs to be as simple as possible. However, even simple models like Smagorinsky, involve gradients of the filtered velocities and test-filtering operations (for the dynamic version). In an effort to circumvent such difficulties, recent modeling efforts focused on employing data-driven approaches. For example, Schoepplein *et al.* [26] used gene-expression programming in order to derive best-fit functional relationships for the unresolved stress tensor using data from direct simulations.

Another nonclassic modeling approach is based on deconvolution. Deconvolution aims to recover an approximation of the original fields from their filtered counterparts. In contrast to (most) classic models, deconvolution methods do not explicitly involve tunable parameters. In principle, such an approach is independent of the flow regime and flow physics. The gradient model, for example, [17] is a form of an approximate deconvolution model, where only the leading term in the Taylor series expansion of the filtering operation is retained. The scale-similarity model is also another example, and it is important to note that these two models form the basis of many mixed models. Approximate deconvolution methods using truncated Taylor series expansions have already been successfully employed to model the unresolved stresses in incompressible and nonreacting flows in previous studies [27–30]. In the case of reacting flows, such approximate deconvolution methods were also assessed, both *a priori* and *a posteriori*, with overall good results [31–34].

In recent studies, more exact iterative algorithms were employed. Wang and Ihme [35] developed a constrained iterative reconstruction algorithm, and performed *a priori* and *a posteriori* studies of a turbulent partially premixed flame interacting with decaying turbulence with impressive results. An iterative reconstruction algorithm was also employed in [36,37] in a substantially different flow configuration, involving a multicomponent fuel flame [38,39] to model the progress variable variance. The same approach was later employed to model the progress variable scalar flux [40]. It is important to note that the DNS database used in these studies involved a highly complex flame structure with a wide heat release zone and overlapping individual species reaction zones [41], thus presenting a stringent test case. Regions of both gradient and countergradient scalar transport were predicted accurately [40], two regimes which are notoriously difficult to model with classic closures. Given these recent advances, it is important to examine whether iterative deconvolution can be successfully used to model the unresolved stress tensor in a demanding flow configuration including both reaction and mean shear.

Even though the focus in this study is on explicit LES formulations, it is important to note that in implicit LES, subgrid-scale (SGS) dissipation may be satisfactorily modeled by the numerical scheme [42–45]. Although explicit modeling is not routinely used in implicit LES, it was suggested in a recent study that additional explicit filtering with a filter size larger than the mesh spacing can improve the dissipation characteristics close to the filter cut-off wave number [46]. Therefore, the benefits of explicit modeling are not necessarily restricted to explicit LES formulations alone, and deconvolution methods are a natural fit in such high-order hybrid LES formulations [46,47].

In this study, a DNS database of a turbulent and reacting shear flow, namely, a rod-stabilized V-flame, is used in order to assess the performance of an iterative deconvolution-based modeling approach for the unresolved stress tensor. The performance of the method is compared to that of eight other classic models such as Smagorinsky, gradient, similarity, and models of the mixed kind, thus presenting one of the most comprehensive model evaluations to date. It is important to note that although *a priori* studies may not guarantee functionality of a model in actual LES, they are detrimental for the clear evaluation of LES closures which cannot be thoroughly assessed in actual LES where the effects of numerical dissipation may overshadow any modeling effects. Sections II and III give details of the DNS database and the data-processing process, Sec. IV gives a brief overview of the modeling problem and the different models tested, and results are presented in Sec. V.

II. DIRECT NUMERICAL SIMULATION DATABASE

The V-flame DNS data used in the present study have been reported in [48], and the methodology and conditions are summarized in this section. The fully compressible governing equations for the conservation of mass, momentum, temperature, and mass fractions of $N_s - 1$ species, where N_s is the total number of species, are solved for using an in-house DNS code (TTX),

$$\frac{\partial \rho}{\partial t} + \nabla \cdot (\rho \boldsymbol{u}) = 0, \tag{1}$$

$$\frac{\partial (\rho \boldsymbol{u})}{\partial t} + \nabla \cdot (\rho \boldsymbol{u}\boldsymbol{u}) = -\nabla \cdot \boldsymbol{P}, \tag{2}$$

$$\begin{aligned}\frac{\partial (\rho T)}{\partial t} + \nabla \cdot (\rho \boldsymbol{u} T) = {} & \frac{1}{\bar{c}_v}\nabla \cdot (\lambda_{th}\nabla T) - \frac{1}{\bar{c}_v}\sum_{i=1}^{N}(\rho Y_i \boldsymbol{V}_i c_{p,i} \cdot \nabla T) - \frac{T}{\bar{c}_v}\sum_{i=1}^{N}[R_i \nabla \cdot (\rho Y_i \boldsymbol{V}_i)] \\ & - \frac{1}{\bar{c}_v}\boldsymbol{P} : (\nabla \boldsymbol{u}) - \frac{1}{\bar{c}_v}\sum_{i=1}^{N}(h_i \omega_i) + \frac{T}{\bar{c}_v}\sum_{i=1}^{N}(R_i \omega_i),\end{aligned} \tag{3}$$

$$\frac{\partial (\rho Y_i)}{\partial t} + \nabla \cdot (\rho \boldsymbol{u} Y_i) = -\nabla \cdot (\rho Y_i \boldsymbol{V_i}) + \omega_i, \tag{4}$$

where λ_{th}, h_i, R_i, and ω_i denote the mixture's thermal conductivity, specific species enthalpy, characteristic gas constant, and reaction rate of species i, respectively. The stress tensor $\boldsymbol{P}$ is given by

$$\boldsymbol{P} = \left[p + \left(\frac{2}{3}\mu - \kappa\right)(\nabla \cdot \boldsymbol{u})\right]\boldsymbol{I} - \mu[(\nabla \boldsymbol{u}) + (\nabla \boldsymbol{u})^T], \tag{5}$$

where μ is the dynamic viscosity and κ is the bulk viscosity of the mixture. The diffusion velocity of species i, $\boldsymbol{V_i}$, is modeled using Fickian-type diffusion. Other symbols have their usual meanings. The equations are discretized on a uniform mesh, using a fourth-order central difference scheme, and are integrated in time using a third-order Runge-Kutta scheme. The chemical source terms are integrated using a point-implicit method in order to reduce stiffness. The adiabatic combustion of a stoichiometric H_2-air mixture at 0.1 MPa is simulated using a detailed kinetic mechanism [49] consisting of 27 elementary reactions and 12 species (H_2, O_2, H_2O, O, H, OH, HO_2, H_2O_2, N_2, N, NO_2, and NO). The temperature dependence of viscosity, thermal conductivity, and diffusion coefficients are taken into account using the CHEMKIN-II packages [50,51], which have been modified for parallel computations. The effects of Soret, Dufour, pressure gradient, and radiative heat transfer are neglected.

The domain is a cuboid, where inflow-outflow boundaries are used in the x direction, an outflow boundary is applied in the z direction, and a periodic boundary is specified in the y (homogeneous) direction. From the inflow boundary, the premixed unburnt mixture and turbulence are fed at the mean velocity $\bar{u}_{in}$. The inflowing turbulence is obtained by performing DNS of incompressible homogeneous isotropic turbulence using a spectral method. In the present DNS, a no-slip flame

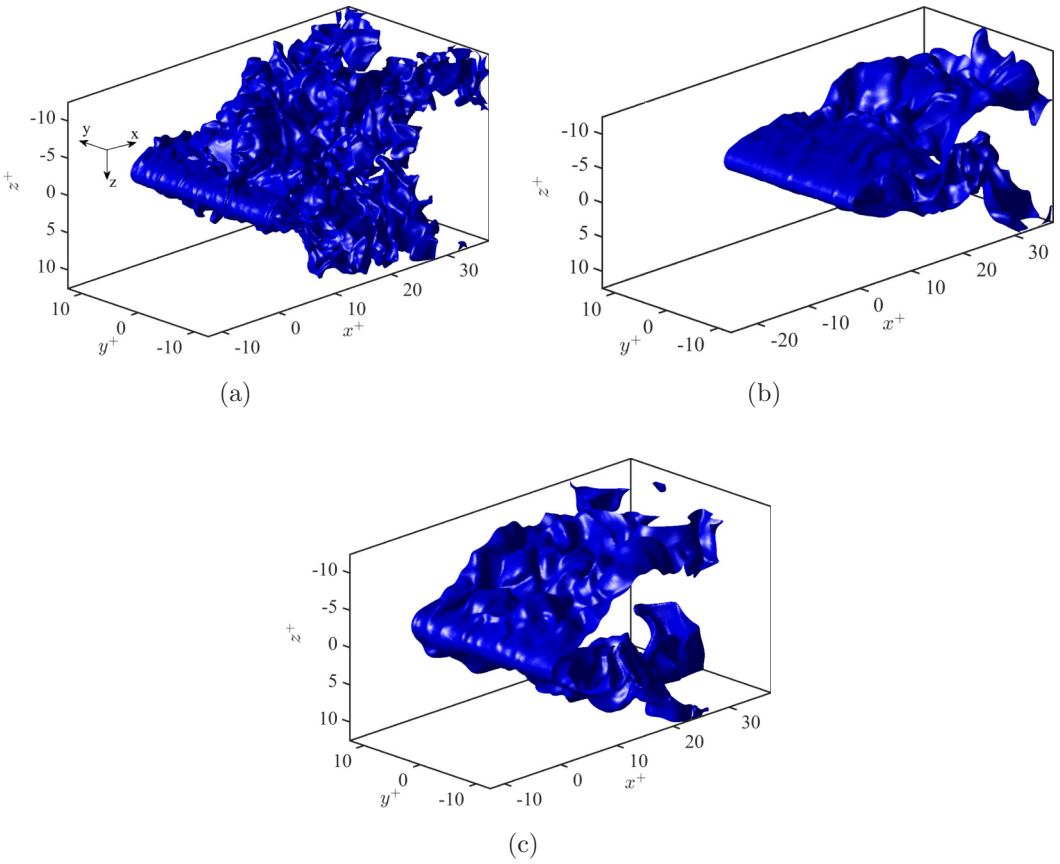

FIG. 1. Progress variable isosurface, $c = 0.1$, for (a) case V97, (b) case V60H, and (c) case V60.

anchor (rod) consisting of a high-temperature region is imposed at a distance x_r from the inflow boundary. The rod diameter $d \simeq \delta_{\text{th}}$, where δ_{th} is the flame thermal thickness (0.49 mm). Within the rod, fixed values are imposed: $T_{\text{rod}} = 2000$ K, $u_{i,\text{rod}} = 0$, and the species mass fractions are set to the products value, i.e., $Y_{k,\text{rod}} = Y_{k,p}$ [48]. These values are smoothly matched to the free-stream values using a Gaussian function [48]. Figure 1 shows an instantaneous progress variable isosurface based on the hydrogen mass fraction, $c = (Y_{\text{H}_2} - Y^r_{\text{H}_2})/(Y^p_{\text{H}_2} - Y^r_{\text{H}_2})$, for the three different cases, and the coordinate system used. Note that the axes are normalized ($^+$) using the laminar flame thickness δ_L (0.2 mm) and are relative to the rod location. Once the simulation has started, the mixture naturally starts reacting and a turbulent flame is established subsequently. After the initialization, the DNS is run for three flow-through times, $L_x/\bar{u}_{\text{in}}$, to ensure that any initial transients have been evacuated. Three V-flames are considered in the present study and their conditions are summarized in Table I. u_{rms} is the root-mean-square value of the fluctuating component of the

TABLE I. Turbulent flame parameters for the DNS studies.

Case	$\bar{u}_{\text{in}}/s_L$	u_{rms}/s_L	Re_d	l_T/δ	Ret	Da	Ka	L_x (mm)	L_y (mm)	L_z (mm)	x_r (mm)
V60	10.0	2.2	614.4	100.0	220.0	45.5	0.33	10.0	5.0	5.0	2.5
V60H	20.0	2.2	1228.7	100.0	220.0	45.5	0.33	12.5	5.0	5.0	5.0
V97	20.0	6.0	1228.7	93.8	562.8	15.6	1.52	10.0	5.0	5.0	2.5

incoming turbulence field, with an integral length scale l_T. The turbulence Reynolds number is $\mathrm{Re}_T = u_{\mathrm{rms}} l_T / \nu_r$, the Damköhler number is $\mathrm{Da} = (l_T/u_{\mathrm{rms}})/(\delta/s_L)$ and the Karlovitz number is $\mathrm{Ka} = (\delta/\eta_k)^2$, where s_L is the laminar flame speed, and the diffusive thickness $\delta = \nu_r/s_L$. The laminar flame thickness is defined as $\delta_L = (Y^r_{\mathrm{H}_2} - Y^p_{\mathrm{H}_2})/\max(dY_{\mathrm{H}_2}/dx)$ where Y_{H_2} is the hydrogen mass fraction profile obtained from a laminar flame calculation. The Reynolds number based on the rod diameter and mean incoming free-stream velocity, $\mathrm{Re}_d = \bar{u}_{in} d/\nu_r$, is also shown in Table I. It is well established that laminar vortex shedding, i.e., Karman vortex streets, are found for up to about Re_d 190 for incompressible, nonreacting flows, and with a relatively low incoming turbulence level [52,53]. Above this limit, instabilities and more chaotic behavior start to appear [53]. The critical Reynolds number where shear layers separate, becoming unstable, is around 1200 according to [54]; however, values ranging from 300 to 3000 were reported [55]. In this case, there is substantial heat release and incoming turbulence which have a direct influence on the vortex dynamics. The shear layers separate from the surface relatively early, and behind the cylinder a recirculation region is established with a substantial turbulence level as noted in [48]. Inside the shear layers where combustion occurs, the mean strain rate is significant and a detailed analysis on the matter is given in [48] (Figs. 5 and 6 in [48]).

The computational domain size, $L_x \times L_y \times L_z$, is $10 \times 5 \times 5$ mm for V60 and V97 and $12.5 \times 5 \times 5$ mm for V60H. The rod is placed at $x_r = 2.5$ mm for cases V60 and V97, and at $x_r = 5.0$ mm for case V60H. These domains are discretized on a uniform mesh $N_x \times N_y \times N_z$ of $513 \times 257 \times 257$ points for V60, $641 \times 257 \times 257$ points for V60H, and $769 \times 385 \times 385$ points for V97. These resolutions ensure that there are at least 20 mesh points inside δ_{th} so that it is well resolved. Also, the resolution for the DNS was found to be more than sufficient to resolve turbulence and the boundary layers near the flame anchor. Figure 2 shows instantaneous y-averaged distributions of the progress variable c for the three different cases. Note the extinction events taking place for case V97 immediately downstream from the rod due to the excessive shear and higher turbulence level.

III. FILTERING/SAMPLING

The DNS data are explicitly filtered on the fine DNS mesh using a Gaussian filter, $G(\underline{x}) = [6/(\pi\Delta^2)]^{3/2} \exp(-6x_i x_i/\Delta^2)$, where Δ is the corresponding filter width. The laminar flame thickness is used as a basis for filtering at $\Delta^+ = \Delta/\delta_L = 1.0$, 2.0, and 3.0. Favre-filtered variables are defined as usual, $\tilde{\phi}(\underline{x}, t) = \overline{\rho\phi}/\bar{\rho}$. In order to simulate an LES, the filtered data are sampled onto a much coarser LES mesh with mesh spacing h, as indicated in Table II. The LES mesh criterion developed in [36] is used, namely, $h/\Delta = 1/4$. This ensures that the filtered progress variable thickness is well resolved on the coarse mesh. This results in LES meshes which are coarser than the Kolmogorov length scale of the incoming turbulence as indicated in Table II: for cases V60 and V60H the ratio h/η_k spans 3.6–10.8 while for case V97 it spans 7.8–23.3. As a result, small-scale information of the order of η_k is not resolved on the simulated LES mesh [36,40]. In contrast to most *a priori* studies in the literature which are conducted on the fine DNS mesh, this presents a more stringent *a priori* evaluation; gradients, for example, in classic models for the stress tensor discussed in the next section, are evaluated on the coarser LES mesh [40]. The DNS data are filtered for a period of more than one flame time $t_{\mathrm{fl}} = t/(\delta_L/s_L)$, and volume-averaged quantities have also been time averaged in order to increase the statistical accuracy of the results.

Figure 3 shows the averaging locations in the streamwise direction along with the distribution of the averaged normal stress component $\langle \tau^+_{11} \rangle$. Note that this component is symmetric around the rod as expected. The stresses are normalized $(^+)$ using the unburnt mixture values ρ_r and s_L. The contour plot in Fig. 3 corresponds to case V60H, and the largest filter width $\Delta^+ = 3$. The streamwise sampling locations are shown in dashed gray lines. These locations span a region of high shear immediately upstream of and downstream from the rod at $-1.5\delta_L$, $0\delta_L$, $1.5\delta_L$, $3\delta_L$, and $5\delta_L$ relative to the rod location. As one may observe from the results in Fig. 2 these locations also span regions with

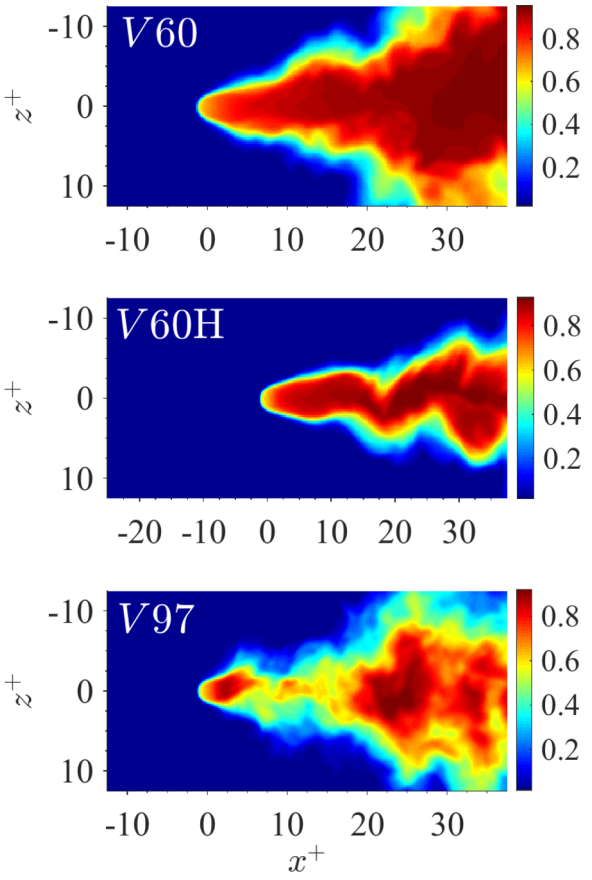

FIG. 2. Averaged (in homogeneous y direction) instantaneous progress variable, $\langle c \rangle$, for all three cases.

a high heat release, and are kept the same for all three DNS cases. Figure 4 shows the orientation of the largest stresses in the two nonhomogeneous directions x and z for clarity.

TABLE II. DNS and LES meshes for $h/\Delta = 1/4$.

Case	Δ^+	N_x	N_y	N_z	h/η_k
V60	0	513	257	257	
	1	201	101	101	3.6
	2	101	51	51	7.1
	3	67	34	34	10.8
V60H	0	641	257	257	
	1	251	101	101	3.6
	2	126	51	51	7.1
	3	83	33	33	10.8
V97	0	769	385	385	
	1	201	101	101	7.8
	2	101	51	51	15.4
	3	67	34	34	23.3

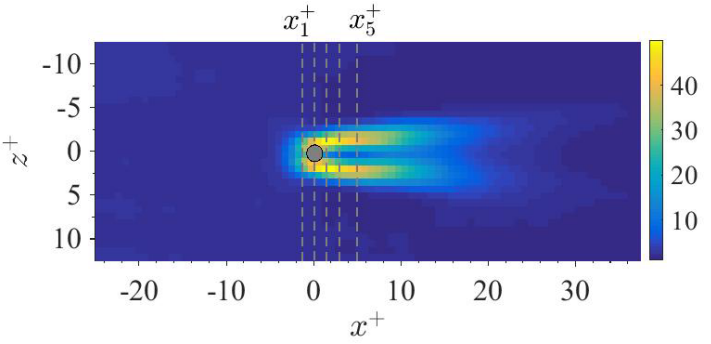

FIG. 3. Averaged (in homogeneous y direction) normal stress component τ_{11}^+, for case V60H and $\Delta^+ = 3$: averaging locations are shown in gray-dashed lines at $x_1^+ = -1.5\,\delta_L, x_2^+ = 0, x_3^+ = 1.5\,\delta_L, x_4^+ = 3\,\delta_L$, and $x_5^+ = 5\,\delta_L$ relative to the rod location for all three DNS cases.

IV. MATHEMATICAL BACKGROUND

The filtered momentum equation for a compressible flow reads

$$\frac{\partial \bar{\rho}\tilde{u}_i}{\partial t} + \frac{\partial \bar{\rho}\tilde{u}_i\tilde{u}_j}{\partial x_j} = -\frac{\partial \bar{p}}{\partial x_i} + \frac{\partial \tau_{ij}^r}{\partial x_j} - \frac{\partial \tau_{ij}}{\partial x_j}, \tag{6}$$

where the resolved and unresolved stress tensors τ_{ij}^r and τ_{ij} are given by

$$\tau_{ij}^r = \overline{\mu\left(\frac{\partial u_i}{\partial x_j} + \frac{\partial u_j}{\partial x_i}\right)} - \frac{2}{3}\delta_{ij}\overline{\mu\frac{\partial u_k}{\partial x_k}}$$

and

$$\tau_{ij} = \bar{\rho}(\widetilde{u_i u_j} - \tilde{u}_i\tilde{u}_j), \tag{7}$$

respectively. The resolved stress tensor is usually approximated using

$$\tau_{ij}^r \simeq \bar{\mu}\left(\frac{\partial \tilde{u}_i}{\partial x_j} + \frac{\partial \tilde{u}_j}{\partial x_i} - \frac{2}{3}\delta_{ij}\frac{\partial \tilde{u}_k}{\partial x_k}\right) = 2\bar{\mu}\left(\tilde{S}_{ij} - \frac{1}{3}\delta_{ij}\tilde{S}_{kk}\right),$$

where

$$\tilde{S}_{ij} = \frac{1}{2}\left(\frac{\partial \tilde{u}_i}{\partial x_j} + \frac{\partial \tilde{u}_j}{\partial x_i}\right)$$

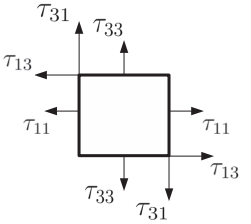

FIG. 4. Orientation of the stresses in the two nonhomogeneous directions for this coordinate system.

is the rate of strain tensor. τ_{ij} is an unclosed term and needs to be modeled. The equation for the total resolved kinetic energy per unit mass, $e = 1/2\tilde{u}_i\tilde{u}_i$, reads

$$\frac{\partial(\bar{\rho}e)}{\partial t} + \frac{\partial(\bar{\rho}\tilde{u}_i e)}{\partial x_i} = -\tilde{u}_i\frac{\partial \bar{p}}{\partial x_i} + \tilde{u}_i\frac{\partial \tau^r_{ij}}{\partial x_j} - \tilde{u}_i\frac{\partial \tau_{ij}}{\partial x_j} \tag{8}$$

and it is clear that the unresolved stress tensor has a direct effect on the evolution of the total resolved kinetic energy (a bulk quantity) through the third term on the right-hand side of Eq. (8), $-\tilde{u}_i\partial\tau_{ij}/\partial x_j$. This term represents energy dissipated or backscattered as a result of unresolved motions. Apart from the Smagorinsky model, the models tested in [1] for the freely propagating turbulent flame included gradient and three similarity-based models, namely, the similarity model of Bardina [19], the similarity model of Vreman [20], and an extended similarity model based on the work of Anderson and Domaradzki [56]. These models were found to have about the same equally better correlation compared to the Smagorinsky model. An alternative progress-variable-based conditional averaging procedure for evaluating the dynamic parameter in the Smagorinsky model was also proposed [1]; however, this did not substantially improve the performance of the model. An important difference with the current DNS database is the presence of a rod which introduces mean shear in the flow [48]. This results in large shear stresses τ_{13} and large normal stresses τ_{11}, in the direction of mean flow. Thus, the current study presents a more stringent evaluation, and in the text which follows the tested models are presented.

A. Smagorinsky

The Smagorinsky model reads [13]

$$\tau_{ij} - \tfrac{1}{3}\delta_{ij}\tau_{kk} = -2\bar{\rho}\nu_t\left(\tilde{S}_{ij} - \tfrac{1}{3}\delta_{ij}\tilde{S}_{kk}\right), \tag{9}$$

where the turbulent viscosity, ν_t, is calculated using $\nu_t = C_D\Delta^2|\tilde{S}|$, where $|\tilde{S}| = \sqrt{2\tilde{S}_{ij}\tilde{S}_{ij}}$. In the static version of the model, the parameter C_D is replaced by C_S^2 where the Smagorinsky constant $C_S \simeq 0.2$. The isotropic contribution [second term on the left-hand side of Eq. (9)] in many LES studies is typically absorbed into the filtered pressure term $\bar{p}$, assuming its contribution is relatively smaller. Erlebacher *et al.* [57] suggested that for relatively small SGS Mach numbers the isotropic contribution of the stress tensor can indeed be neglected. Our focus in this study is modeling the unresolved stress tensor regardless of the size of the isotropic part. In this study, the Yoshizawa approximation is used in order to explicitly model the trace of the stress tensor [58],

$$\tau_{kk} = 2\bar{\rho}C_I\Delta^2|\tilde{S}|^2. \tag{10}$$

In the static version, the model parameter C_I is a constant. Yoshizawa suggested a value of $\simeq$0.089 [58]; however, values ranging from 0.0025 to 0.009 were reported while dynamically evaluating C_I in the study of Moin *et al.* [13]; here we use 0.089 as originally suggested, which was also found to produce quantitatively good results. In the dynamic version, C_I is calculated using [13]

$$C_I = \frac{\langle L_{kk}\rangle}{\langle P\rangle}, \tag{11}$$

where $\langle\cdot\rangle$ indicates an averaging process, and L_{kk} is the trace of the Leonard term,

$$L_{ij} = \widehat{\bar{\rho}\tilde{u}_i\tilde{u}_j} - \widehat{(\bar{\rho}\tilde{u}_i)}\widehat{(\bar{\rho}\tilde{u}_j)}/\hat{\bar{\rho}}.$$

The "hat"ˆindicates test filtering with a filter $\hat{\Delta}$. The ratio $\gamma = \hat{\Delta}/\Delta = 2$ throughout this study. The term P is given by

$$P = 2(\hat{\bar{\rho}}\hat{\Delta}^2|\hat{\tilde{S}}|^2 - \Delta^2\widehat{\bar{\rho}|\tilde{S}|^2}).$$

The dynamic parameter C_D is calculated following the least-squares approach suggested by Lilly [59], using [15]

$$C_D = \frac{\left\langle -\left(L_{ij} - \frac{1}{3}\delta_{ij}L_{kk}\right)M_{ij}\right\rangle}{\langle 2\Delta^2 M_{ij}M_{ij}\rangle}, \tag{12}$$

where

$$M_{ij} = \alpha^2\hat{\bar{\rho}}|\hat{\tilde{S}}|\left(\hat{\tilde{S}}_{ij} - \tfrac{1}{3}\delta_{ij}\hat{\tilde{S}}_{kk}\right) - \left(\widehat{\bar{\rho}|\tilde{S}|\tilde{S}_{ij}} - \tfrac{1}{3}\delta_{ij}\widehat{\bar{\rho}|\tilde{S}|S_{kk}}\right). \tag{13}$$

In accordance with the classic regularization approach [13] C_D is regularized by volume averaging ($\langle\cdot\rangle$) in the homogeneous (y) directions.

B. Scale similarity

The scale-similarity model of Bardina (SIMB) [19] is given by

$$\tau_{ij} = \bar{\rho}(\widetilde{\bar{u}_i\tilde{u}_j} - \widetilde{\bar{u}_i}\widetilde{\tilde{u}_j}). \tag{14}$$

This model showed improved predictions in comparison to the static Smagorinsky model for freely propagating flames [1]. In [1] the following model based on the interscale energy transfer model of Anderson and Domaradzki [56] was also proposed (SIMET);

$$\tau_{ij} = \bar{\rho}(\widehat{\hat{\bar{u}}_i\tilde{u}_j} + \widehat{\hat{\bar{u}}_j\tilde{u}_i} - \hat{\bar{u}}_i\hat{\bar{u}}_j - \widehat{\hat{\bar{u}}_j\hat{\bar{u}}_i}). \tag{15}$$

An important property of the above model is Galilean invariance for the compressible case.

C. Gradient model

The gradient model (GRAD) can be derived by expanding in Taylor series the filtered velocity product in the expression for τ_{ij} [18] and retaining the leading term in the expansion [17],

$$\tau_{ij} = \bar{\rho}\frac{\Delta^2}{12}\frac{\partial\tilde{u}_i}{\partial x_k}\frac{\partial\tilde{u}_j}{\partial x_k}. \tag{16}$$

In [40] the scalar version of this model was used to model the scalar flux term for freely propagating flames, $f_i = (\bar{\rho}\Delta^2/12)(\partial\tilde{u}_i/\partial x_k)(\partial c/\partial x_k)$. In comparison to Iterative Deconvolution Explicit Filtering (IDEF), the model was found to underpredict the scalar flux particularly for the highest turbulence level cases [40]. Nevertheless, the gradient model is well known to perform well in *a priori* studies and it is worthwhile to compare its performance for modeling the stress tensor.

D. Clark model

Vreman *et al.* [18] built upon the mixed model of Clark [17] (CLARK) and produced the following dynamic mixed model with an eddy-diffusivity component complementing the gradient part in order to provide the necessary dissipation,

$$\tau_{ij} = \bar{\rho}\frac{\Delta^2}{12}\frac{\partial\tilde{u}_i}{\partial x_k}\frac{\partial\tilde{u}_j}{\partial x_k} - C_C\bar{\rho}\Delta^2|\tilde{S}'|\tilde{S}'_{ij}, \tag{17}$$

where

$$S'_{ij}(\underline{\tilde{u}}) = \frac{\partial\tilde{u}_i}{\partial x_j} + \frac{\partial\tilde{u}_j}{\partial x_i} - \frac{2}{3}\delta_{ij}\frac{\partial\tilde{u}_k}{\partial x_k} = 2\left(\tilde{S}_{ij} - \frac{1}{3}\delta_{ij}\tilde{S}_{kk}\right) \tag{18}$$

and $|S'| = (0.5S'_{ij}S'_{ij})^{1/2}$. In the static version, the model parameter $C_C = 0.17^2$. In the dynamic version, it is calculated using

$$C_C = \frac{\langle M_{ij}(L_{ij} - H_{ij})\rangle}{\langle M_{ij}M_{ij}\rangle}. \tag{19}$$

Denoting $v_i = \widehat{\bar{\rho}\tilde{u}_i}/\hat{\bar{\rho}}$, the tensors H_{ij} and M_{ij} are given by

$$H_{ij} = \hat{\bar{\rho}}\frac{\hat{\bar{\Delta}}^2}{12}\frac{\partial v_i}{\partial x_k}\frac{\partial v_j}{\partial x_k} - \frac{\Delta^2}{12}\widehat{\left(\bar{\rho}\frac{\partial \tilde{u}_i}{\partial x_k}\frac{\partial \tilde{u}_j}{\partial x_k}\right)}$$

and

$$M'_{ij} = -\hat{\bar{\rho}}\hat{\bar{\Delta}}^2|S'(\underline{v})|S'_{ij}(\underline{v}) + \Delta^2\widehat{[\bar{\rho}|S'(\tilde{\underline{u}})|S'_{ij}(\tilde{\underline{u}})]},$$

respectively. This model was evaluated both *a priori* and *a posteriori*, for the temporal mixing layer (nonreacting), with overall good results [18]. In particular, in [20] this model was compared against the dynamic Smagorinsky, and the dynamic mixed model of Zhang *et al.* [60]. The dynamic mixed model of Zhang *et al.* [60] is of a similar nature but employs instead a scale-similarity term as the base model. The dynamic Clark model showed improved predictions over the dynamic Smagorinsky model, and equally good predictions to the scale-similarity-based model [60] albeit at a lower computational cost. Hence it serves as a good benchmark model in this study.

E. WALE

A similarity-based mixed model, based on the WALE model [21] was proposed in [61]. This model was used to simulate a wall-impinging jet with overall good results [61],

$$\tau_{ij} - \tfrac{1}{3}\delta_{ij}\tau_{kk} = -2\bar{\rho}\nu_t\left(\tilde{S}_{ij} - \tfrac{1}{3}\delta_{ij}\tilde{S}_{kk}\right) + \bar{\rho}(\widehat{\tilde{u}_i\tilde{u}_j} - \hat{\tilde{u}}_i\hat{\tilde{u}}_j). \tag{20}$$

This model has an eddy-diffusivity component like the Smagorinsky model; however, the turbulent viscosity is calculated from the velocity gradient and shear rate tensors using

$$\nu_t = (C_W\Delta)^2\frac{\left(\tilde{s}^d_{ij}\tilde{s}^d_{ij}\right)^{3/2}}{(\tilde{S}_{ij}\tilde{S}_{ij})^{5/2} + \left(\tilde{s}^d_{ij}\tilde{s}^d_{ij}\right)^{5/4}}.$$

The model constant $C_W = 0.5$, and $\tilde{s}^d_{ij}$ is the traceless symmetric part of the squared resolved velocity gradient tensor $\tilde{g}_{ij} = \partial\tilde{u}_i/\partial x_j$,

$$\tilde{s}^d_{ij} = \tfrac{1}{2}\left(\tilde{g}^2_{ij} + \tilde{g}^2_{ji}\right) - \tfrac{1}{3}\delta_{ij}\tilde{g}^2_{kk},$$

where $g^2_{ij} = g_{ik}g_{kj}$. Note that in this case as well, the static Yoshizawa closure is used to model the trace of the stress tensor. Also, in all models involving test-filtering operations the ratio $\gamma = 2$ is kept the same throughout.

F. IDEF

Deconvolution-based models aim to invert the filtering operation in order to obtain estimates of the unfiltered fields. This can be accomplished with a variety of methods. In [27] a high-order polynomial inversion of the top-hat filter was used which led to the development of generalized and improved similarity models for the unresolved stress tensor. Deconvolution using iterative algorithms, namely, Van Cittert iterations, were successfully employed in [29] to model the unresolved stresses in *a posteriori* studies of decaying and compressible turbulence. In [30] the same approach was used in *a posteriori* LES of turbulent channel flow, and in [62] in LES of transitionary flow. The deconvolution-based model in this study also relies on Van Cittert's iterative reconstruction algorithm, along with an error controller [36], which approximates the unfiltered field by a truncated series expansion of the inverse filtering operation. For a filtered field $\bar{\phi}$ the algorithm reads

$$\phi^{*n+1} = \phi^{*n} + b(\bar{\phi} - G * \phi^{*n}), \tag{21}$$

where $\phi^{*0} = \bar{\phi}$, and ϕ^* is the approximation of the unfiltered field for a given iteration count. In the case $\phi = \rho u_i$ and $\phi = \rho$ with $b = 1$ (typical value), the first two iterations result in the following

approximations for the unfiltered density and density-velocity product,

$$\rho^{*0} = \overline{\rho}, \quad \rho^{*1} = 2\overline{\rho} - \overline{\overline{\rho}}, \quad \{\rho u_i\}^{*0} = \overline{\rho u_i}, \quad \{\rho u_i\}^{*1} = 2\overline{\rho u_i} - \overline{\overline{\rho u_i}}.$$

The nth approximation of $\rho u_i u_j$ is calculated using $\{\rho u_i u_j\}^{*n} = \{\rho u_i\}^{*n}\{\rho u_j\}^{*n}/\rho^{*n}$, and the corresponding approximation of the unresolved stress tensor is calculated using $\tau_{ij}^n = \bar{\rho}(\overline{\{\rho u_i u_j\}^{*n}}/\bar{\rho} - \tilde{u}_i\tilde{u}_j)$. It is straightforward to show that the first two are

$$\tau_{ij}^0 = \overline{\bar{\rho}\tilde{u}_i\tilde{u}_j} - \bar{\rho}\tilde{u}_i\tilde{u}_j,$$

$$\tau_{ij}^1 = \overline{\left(\frac{4\overline{\rho u_i}\rho u_j - 2\overline{\rho u_i}\,\overline{\rho u_j} - 2\overline{\rho u_j}\,\overline{\rho u_i} + \overline{\overline{\rho u_i}\,\overline{\rho u_j}}}{2\bar{\rho} - \bar{\bar{\rho}}}\right)} - \bar{\rho}\tilde{u}_i\tilde{u}_j.$$

Note that for $n = 0$, a Bardina-like similarity model is recovered. The same result is actually obtained by using the decomposition $\phi = \bar{\phi} + \phi'$ for the density and velocity fields in the expression for τ_{ij}, and assuming any fluctuations $\phi' = 0$. This is equivalent to assuming that the unfiltered field is approximated by the filtered field. For $n = 1$, an extended model is obtained involving double and triple-filtered quantities and so on for higher-order approximations. The algorithm is a linear one, and for periodic signals it is straightforward to show that for a sufficiently large number of iterations, and provided $0 < b < 2$, the algorithm is stable and converges to the original value of the unfiltered field [36,40] for all finite wave numbers on the mesh. A more in-depth analysis on convergence rates and error bounds for the Van Cittert algorithm is given in [63]. b is typically taken to equal 1 for nonoscillatory convergence as shown in [40]. The maximum number of iterations required for a sufficiently small reconstruction error, depends on the largest wave number resolved by the mesh. In practice, a maximum number of iterations N_{itr} are set *a priori*, and a controller is used measuring the error between the filtered and filtered-deconvoluted fields. As long as the error decreases with iteration count, the iterations continue until the maximum number of iterations is reached and the algorithm exits. This implementation gave quantitatively good reconstructions of scalar fields (density and progress variable) in [36], and of velocity fields in [40], and is also employed in this study. Further details of the implementation are given in [36]. Successive iterations lead to higher-order approximations of the unfiltered fields and of the unresolved stress tensor as shown in [30]. For example, four iterations are sufficient to recover the gradient model supplemented by the next term in the series [Eq. (B9) in [29]]. Deconvolution has also been successfully used in LES of reacting flows. In [32] an approximate deconvolution method was used to recover estimates of the unfiltered progress variable field which was used to close the filtered source term in the transport equation for the filtered progress variable. In [35], a constrained deconvolution method was employed for modeling turbulent partially premixed flames, and was shown to successfully reconstruct scalar fields and flux terms. In the same study [35], *a posteriori* testing using LES was also conducted with overall good results.

In comparison to the rest of the models, the IDEF approach is straightforward to implement since the algorithm is relatively simple and only involves successive filtering operations, with no gradient calculations or the evaluation of any dynamic parameters which typically require the evaluation of fractions [e.g., Eqs. (11), (12), and (19)]. As a result, from an implementation point of view IDEF is a more robust modeling method.

V. MODEL PERFORMANCE EVALUATION

From the foregoing discussion it becomes clear that the static Smagorinsky, dynamic Smagorinsky, similarity, and gradient models are the four fundamental ingredients of more complex models. Table III, lists the main properties of these models, and a more in-depth discussion on the subject is given in [64].

TABLE III. Some of the fundamental classic stress-tensor models with their underlying assumptions and limitations.

Model	Assumptions/Limitations
Static Smagorinsky (S-SMAG) [2]	
	τ_{ij} aligned with $\tilde{S}_{ij}$.
	Purely dissipative, no backscatter.
	τ_{kk} not modeled (additional closure required).
	Typically low correlation coefficients in *a priori* tests.
	Not recommended for shear and transitional flows.
	Poor correlations in reacting flows [1].
Dynamic Smagorinsky (D-SMAG) [12,13]	
	τ_{ij} aligned with $\tilde{S}_{ij}$.
	Dissipation and backscatter depending on sign of C_D.
	τ_{kk} not modeled.
	Improved performance in LES.
	Regularization sensitive to flow configuration/geometry.
	Classic regularization inadequate for reacting flows [1].
	Poorer correlations than S-SMAG for reacting flows [1].
Similarity-Bardina (SIMB) [19]	
	Scale-invariance hypothesis.
	Dissipation and backscatter.
	τ_{kk} modeled.
	Improved correlation coefficients for reacting flows [1].
	Sensitive to ratio $\gamma = \hat{\Delta}/\Delta$.
	Insufficient dissipation in actual LES.
	Typically used in mixed models.
Gradient [17]	
	Filters with finite second moments required.
	Dissipation and backscatter.
	τ_{kk} modeled.
	Improved correlation coefficients in reacting flows [1].
	Insufficient dissipation in actual LES.
	Typically used in mixed models.

As pointed out in the Introduction, the evaluation of dynamic parameters requires a robust regularization procedure. In the case of the Smagorinsky model, two parameters can be evaluated dynamically, C_I and C_D, leading essentially to four different model formulations. In this study, it was found that the standard process of averaging in the homogeneous directions resulted in sharp spatial gradients for both of these quantities, particularly for C_I. Figure 5 shows normalized histograms of the instantaneous distributions of the numerator $\langle L_{kk}^{+} \rangle$, and denominator $\langle P^{+} \rangle$ in Eq. (11) used to calculate C_I. The distributions correspond to case V97, and $\Delta^{+} = 3$. Similar distributions were obtained for the rest of the cases and are not shown here. The superscript $+$ denotes quantities normalized using the unburnt mixture laminar flame values, ρ_r and s_L. While the numerator $\langle L_{kk} \rangle$ remains positive, the denominator $\langle P \rangle$ is predominantly negative, and this change in sign resulted in sharp spatial gradients while evaluating C_I, which deteriorated the normal stress predictions using the dynamic Yoshizawa approximation. Negative P values were also reported for freely propagating flames [1]. In an effort to remedy this, an alternative averaging formulation was suggested, $C_I = \langle L_{kk} P \rangle / \langle P^2 \rangle$ [1]. This regularization process was also tested in this study, but was not found to improve the results. As a result, only C_D is evaluated dynamically.

Figure 6 shows the overall Pearson correlation coefficients for each component of the stress tensor. The Pearson coefficients are averaged over all three filter widths and over all three DNS

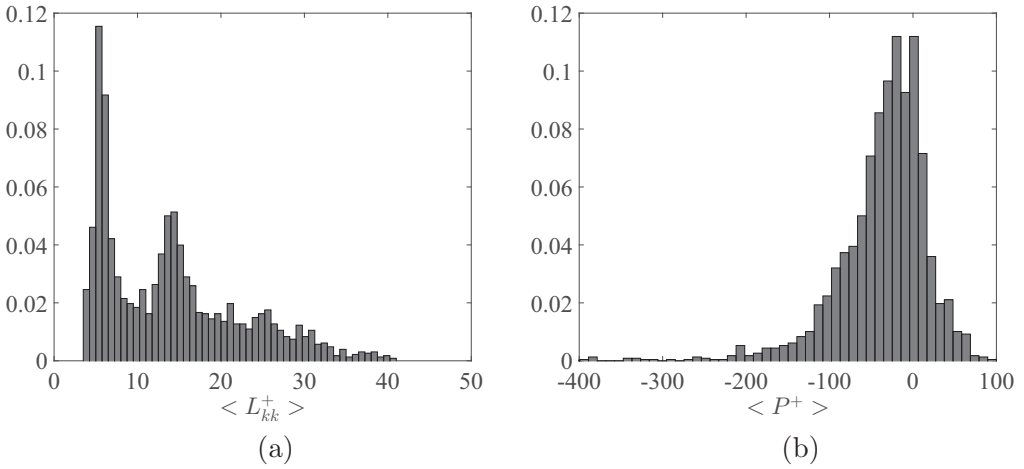

FIG. 5. Normalized histograms of instantaneously averaged values of (a) numerator $\langle L_{kk} \rangle$ and (b) denominator $\langle P \rangle$, used to calculate dynamic parameter C_I in Eq. (11) (case V97, $\Delta^+ = 3$).

cases, in order to obtain a global performance metric. The static Smagorinsky (S-SMAG) and dynamic Smagorinsky (D-SMAG) models have the lowest correlation coefficients, with magnitudes of the same order as those reported for freely propagating flames [1]. These low correlation coefficients are a result of the Boussinesq assumption failing for reacting flows as noted in previous experimental and numerical studies [1,23]. Figure 6 shows that the predictions for τ_{12}, τ_{23}, and τ_{32} deteriorate for the dynamic model, while they improve only for the relatively larger stress component τ_{13}. Overall, however, the Pearson coefficients both for the static and dynamic models are less than $\simeq$0.4. When compared to the rest of the models, it is clear that both the static and dynamic versions are not recommended for application in reacting flows, a point which was also noted in [1]. In order to elucidate the sensitivity of the models to filter width (and mesh spacing) variations, filter-specific Pearson coefficients averaged over all six stress tensor components are shown in Fig. 7. The static Smagorinsky model appears to be relatively insensitive to variations in filter width, as does the deconvolution-based model (IDEF). The rest of the models exhibit some sensitivity, particularly the D-SMAG, SIMET, D-CLARK, and WALE models. It is interesting to note that these models all involve test-filtering operations: the scale-similarity assumption may be

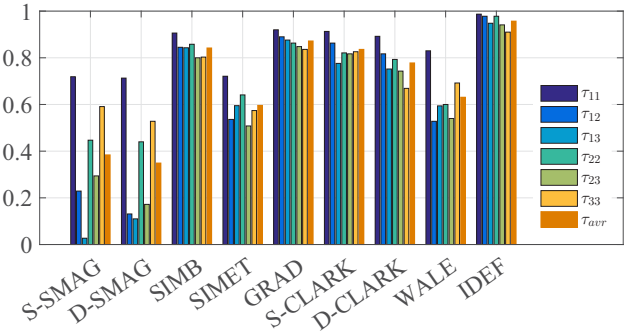

FIG. 6. Pearson correlation coefficients averaged across all cases and all filter widths, for individual stress-tensor components.

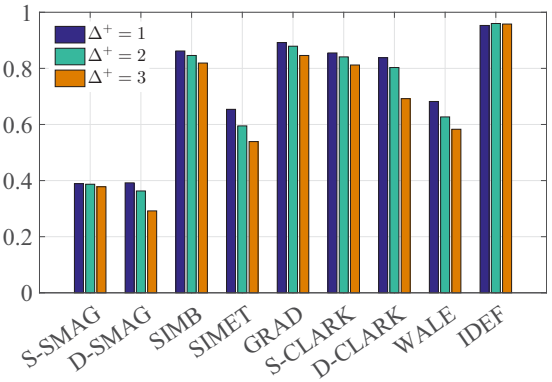

FIG. 7. Pearson correlation coefficients averaged across all stress-tensor components and all cases, for individual filter widths.

violated at the test-filter level causing this sensitivity for the largest filters. Overall, of all the models tested, the similarity, gradient, and IDEF models have some of the highest correlation coefficients.

In order to elucidate the effect of iteration count N_{itr} on the performance of the IDEF approach, mean Pearson correlation coefficients (averaged over all six components of the stress tensor) have been calculated for case V97 and $\Delta^+ = 3$, and these are shown in Fig. 8. After about ten iterations, there is little improvement in the correlation which implies this is a good upper bound for this method. This bound is also in accordance with previous *a priori* but also *a posteriori* studies in the literature for substantially different flow regimes involving nonreacting and incompressible shear flows [29,30]. Nevertheless, in this study the maximum iteration count was set to 30 for all cases. This choice is also the computationally most demanding one, and will serve as a good case for comparing with the rest of the models (discussed later in the text).

In order to further quantify the performance of the models, spatial averages have been calculated for the largest stress components for this flow configuration, namely, $\langle \tau_{11} \rangle$ and $\langle \tau_{13} \rangle$. Figures 9 and 10 show the streamwise predictions for the normal and shear stresses for $\Delta^+ = 1$ and 3, respectively, for the highest turbulence level case V97. Similar distributions were obtained for cases V60 and V60H and are not shown here. Significant differences are observed in the models' predictions particularly for the largest filter width. The static and dynamic versions of the Smagorinsky model give reasonable normal stress predictions for $\Delta^+ = 1$. The rest of the

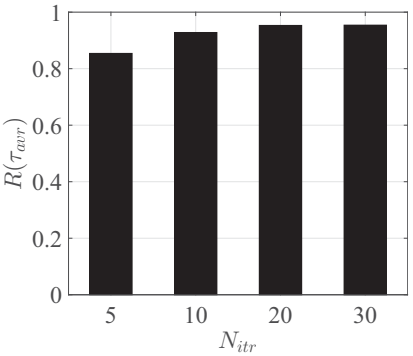

FIG. 8. Pearson coefficient averaged over all six stress-tensor components for different number of iterations using the IDEF method, for case V97 and $\Delta^+ = 3$.

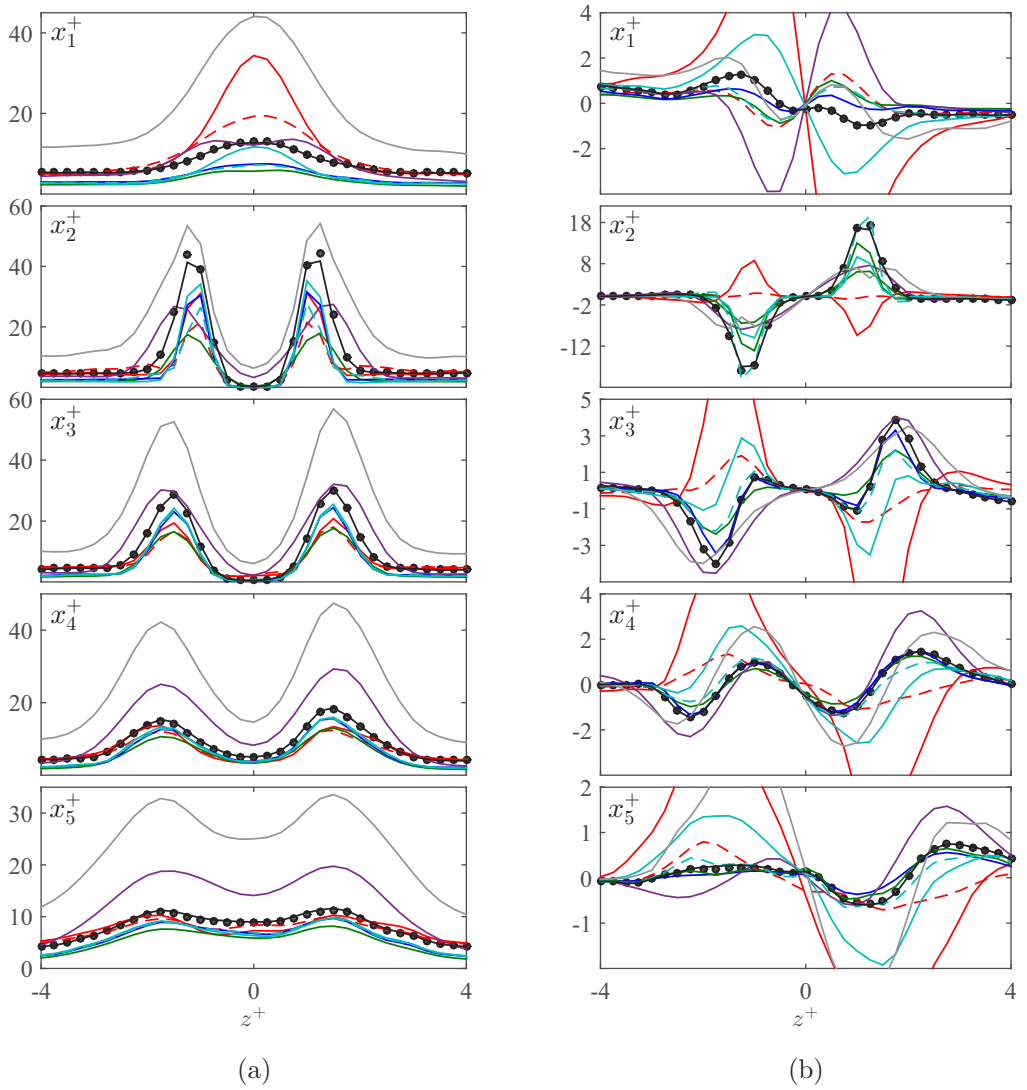

FIG. 9. Average shear stresses (a) $\langle \tau_{11}^+ \rangle$ and (b) $\langle \tau_{13}^+ \rangle$, for different x locations, case V97, $\Delta^+ = 1.0$: •, DNS; —— S-SMAG, - - - D-SMAG —— SIMB, —— SIMET, —— GRAD, —— S-CLARK, - - - D-CLARK-D, —— WALE, —— IDEF.

models give equally good predictions apart from the WALE model which somewhat overpredicts the normal stresses particularly downstream from the rod for $-2 < z^+ < 2$ approximately. Of the two similarity-based models, the SIMB model performs better, with the SIMET model overpredicting the normal stress particularly in the wake/shear region downstream from the rod. The predictions for the shear stress component τ_{13} are substantially different between the models even for the smallest filter width. The dynamic Smagorinsky model improves the predictions for τ_{13} as evidenced by the larger correlation coefficient for this component in Fig. 6. In general, however, both the static and dynamic versions of the Smagorinsky model perform poorer in comparison to the rest of the models: the static version in particular predicts an opposite sign of the shear stress immediately downstream from the rod at $x^+ = 3$. In order to shed some light on this, Fig. 11 shows instantaneous y-averaged values of the actual shear stress component τ_{13}, the modeled stress using the dynamic

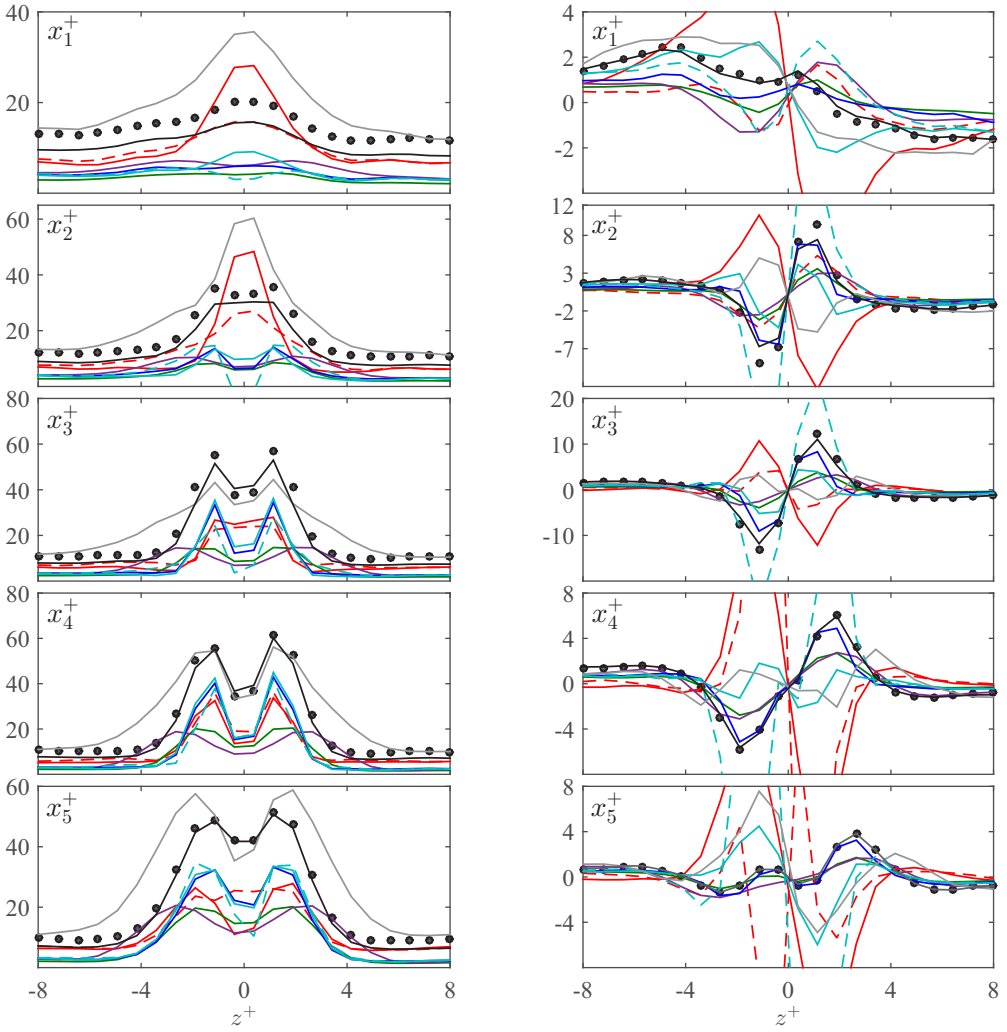

FIG. 10. Average shear stresses (a) $\langle \tau_{11}^+ \rangle$ and (b) $\langle \tau_{13}^+ \rangle$, for different x locations, case V97, $\Delta^+ = 3.0$. Lines as in Fig. 9.

Smagorinsky model, and the rate of strain tensor $\tilde{S}_{13}$, at streamwise location x_3^+ and for $\Delta^+ = 3$. These variables are normalized (n) using their corresponding maximum values. The variation of the dynamic parameter C_D normalized using the static value of the parameter (0.2^2) is also shown. In the static version of the model, this shear stress component is given by $\tau_{13} = -2\bar{\rho}C_S^2\Delta^2|\tilde{S}_{ij}|\tilde{S}_{13}$, hence in regions where the rate of strain is positive, a negative shear stress is predicted, while in regions where it is negative a positive stress is predicted. In the case of the dynamic model, C_S^2 is replaced by C_D, and the situation somewhat improves since $|C_D| < 1$ in this region which reduces the absolute value of the shear stress in this region. Even so, in regions where the rate of strain is predominantly negative, i.e., for $-2 < z^+ < 0$ approximately, C_D is still positive, which results in a positive prediction for τ_{13}. Furthermore, C_D remains positive in the region $0 < z^+ < 1.8$ approximately, while the rate of strain tensor is negative, which results in an opposite shear stress prediction relative to the actual stress. This behavior is a direct consequence of the alignment

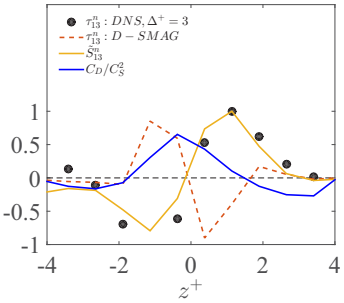

FIG. 11. Instantaneously averaged actual shear stress $\langle \tau_{13} \rangle$, modeled stress, rate of strain tensor $\langle \tilde{S}_{13} \rangle$, and dynamic Smagorinsky parameter $\langle C_D \rangle$: case V97, $\Delta^+ = 3$, at x_3^+.

assumption between the stress and rate of strain tensors in models of this kind which was shown to be invalid in previous studies both for nonreacting [7,8] and reacting flows [1]. Of the remaining models, the SIMET model performs poorer relative to the SIMB model for both filter widths. The D-CLARK model improves the predictions over its static version for $\Delta^+ = 1$, but these predictions deteriorate for $\Delta^+ = 3$. The gradient model gives reasonable predictions, while the IDEF model gives the best overall agreement with the DNS data for both the normal and shear stresses.

In order to elucidate the performance of the top-scoring models between the different DNS cases, Figure 12 shows the predictions of the SIMB, GRAD, and IDEF models for all three DNS cases, for the shear stress τ_{13}. The predictions correspond to the demanding streamwise location x_3^+ which is immediately downstream from the rod, and where the shear stresses are found to be the largest. Figure 12 shows that IDEF performs well across all three cases, i.e., irrespective of the turbulence level and filter width. The SIMB and GRAD models also perform well; however, as one may observe from the results in Figs. 9 and 10 they do not perform as well as IDEF

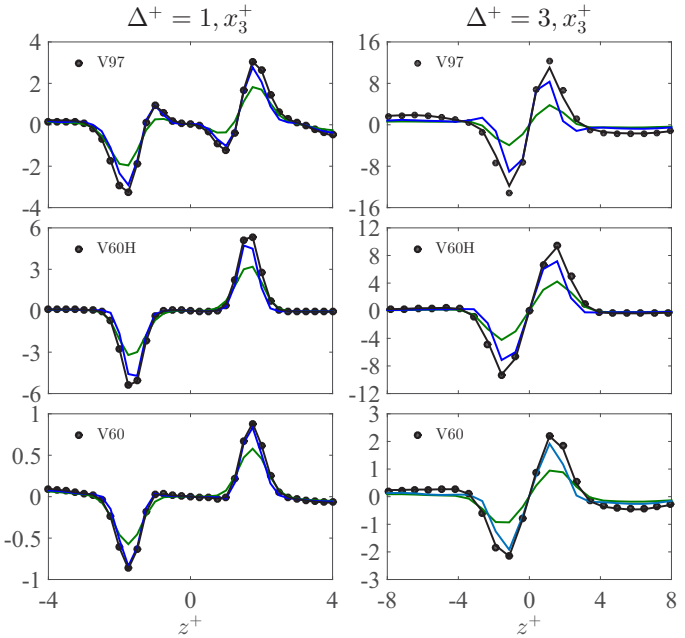

FIG. 12. Average shear stress $\langle \tau_{13}^+ \rangle$ for cases V60, V60H, and V97 at streamwise position x_3^+. Lines as in Fig. 9.

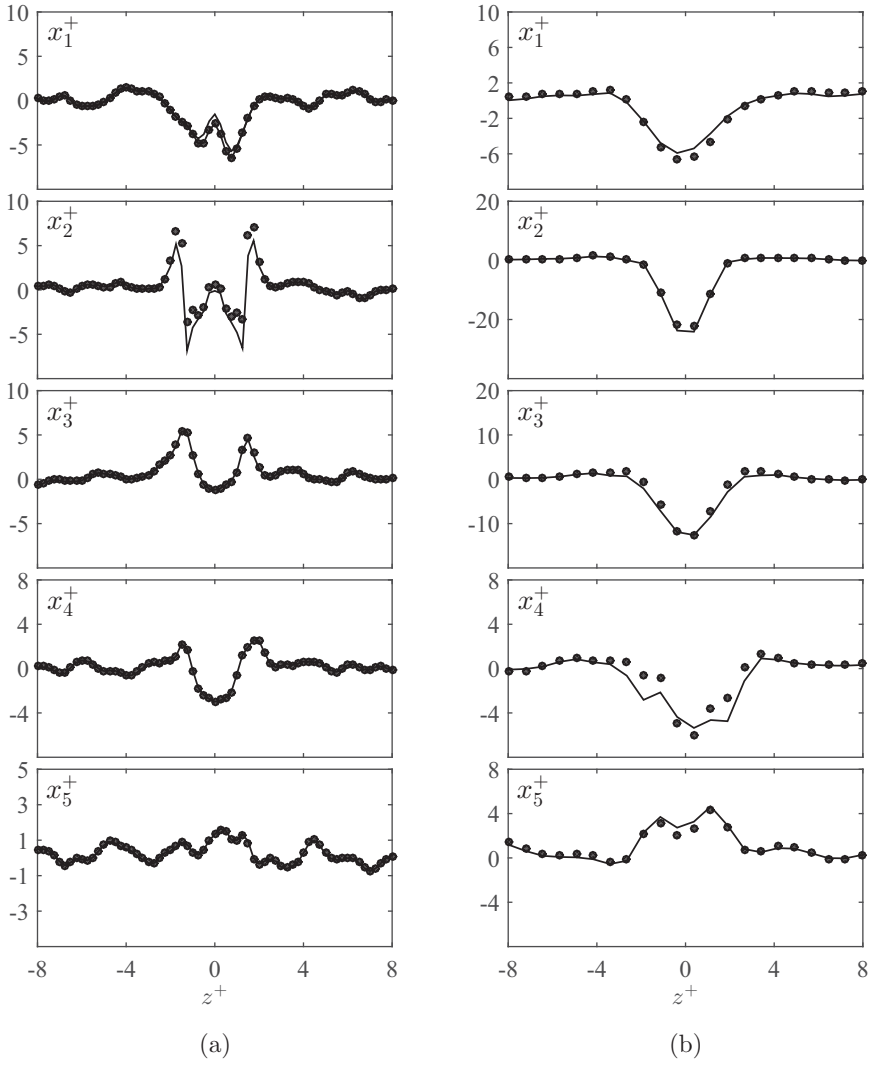

FIG. 13. Average dominant component of the divergence of the stress tensor $\langle f_1^+ \rangle = \langle \delta_L \partial \tau_{1j}^+ / \partial x_j \rangle$ for case V97: (a) $\Delta^+ = 1$, (b) $\Delta^+ = 3$; •, DNS, ——IDEF.

for other streamwise locations. It is important to note that in actual LES, the divergence of the modeled stress tensor, $f_i = \partial \tau_{ij} / \partial x_j$, is a dominant term for the evolution of the flow according to Eq. (6). This term involves gradient calculations and therefore depends on the LES mesh size. Figure 13 shows the dominant component of the divergence for this flow configuration, f_1, obtained using the IDEF-modeled stress tensor against the DNS result. The plots correspond to the most stringent test case, i.e., the highest turbulence level case V97, for $\Delta^+ = 1$ and 3. The divergence is accurately predicted at all streamwise locations, and an equally good agreement was observed for f_2 and f_3 also. A good agreement for the divergence was also demonstrated in [40] for the IDEF-modeled scalar flux term. These results combined, suggest that the reconstructed fields are adequately resolved on the LES mesh in terms of obtaining accurate estimates of the divergence. As a further test, the alignment angle θ between the actual and modeled resultant stresses τ_{j1} and τ_{j1}^m have been calculated for the different models. The alignment angles are expected to be poorest for the largest filter width, and these are shown in Fig. 14 for the different DNS cases at streamwise

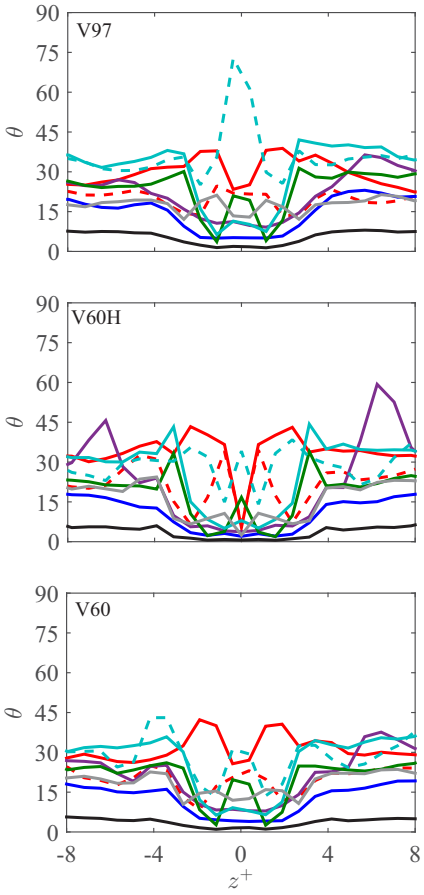

FIG. 14. Alignment angle between modeled τ_{j1}^m and actual τ_{j1}, for $\Delta^+ = 3$, at x_3^+. Lines as in Fig. 9.

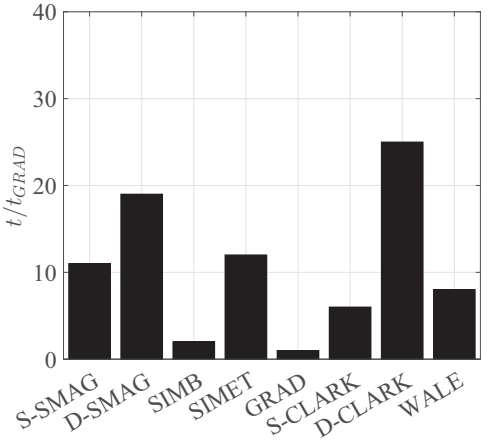

FIG. 15. Normalized wall-clock times for modeling the unresolved stress tensor for all models: case V97, $\Delta^+ = 3$.

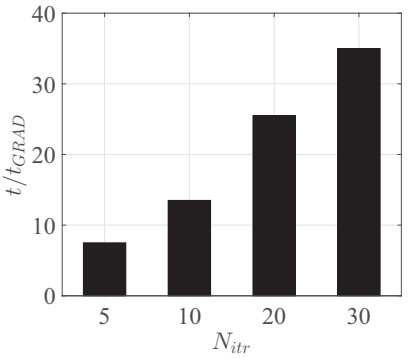

FIG. 16. Normalized wall-clock times for modeling the unresolved stress tensor against iteration count for IDEF: case V97, $\Delta^+ = 3$.

position x_3^+. The dynamic Smagorinsky model improves the alignment significantly in the wake region $-4 < z^+ < 4$. This is owed primarily to the improved τ_{13} predictions as evidenced by the higher correlation coefficient for this stress component in Fig. 6. The dynamic Clark model is found to perform poorer than its static version in this region. This is also consistent with the somewhat poorer correlation coefficients for τ_{13} observed for this model in Fig. 6. The SIMB, GRAD, and WALE models have reasonable alignment angle predictions with the SIMB model having the best alignment, while the SIMET model is generally found to perform poorer in comparison. The deconvolution-based model has the best alignment characteristics for all three cases, while its performance is consistent across the different turbulence levels.

In actual LES, a model for the unresolved stress tensor is also required to be computationally efficient. Figures 15 and 16 show the normalized wall-clock times for each of the eight classic models and for the IDEF model, respectively. These correspond to the time required to model all six components of the stress tensor, for case V97 and $\Delta^+ = 3$. The times are normalized with respect to the fastest model, which was found to be the gradient model. At ten iterations, the average Pearson coefficient for IDEF is 0.93 (Fig. 8). This correlation is much larger than the top-scoring model (GRAD), which has an average Pearson coefficient of 0.84 for the same case and filter width (Fig. 7). At 30 iterations, the compute time is larger than the rest of the classic models, however of the same order of magnitude as that of the dynamic Clark model. At ten iterations, IDEF is found to be faster than the dynamic Smagorinsky model while having a higher correlation coefficient as one may observe from the results in Figs. 7 and 8. These results indicate that IDEF is within reach for practical implementations in LES with timings comparable to those of classic models. Furthermore, given that hybrid architectures are increasingly being used in computational fluid dynamics, IDEF is ideal for offloading to a graphics processing unit as it involves only convolution operations.

VI. CONCLUSIONS

A three-dimensional direct numerical simulation database of a turbulent premixed V-flame is used in order to assess the performance of a deconvolution-based model for the unresolved stress tensor. Previous *a priori* studies for freely propagating flames showed the method to be robust and accurate for modeling the progress variable variance [36] and scalar flux [40], which are two substantially different terms. The flow configuration in this study is substantially more demanding, as it includes both mean shear and reaction, and so is the unresolved term which is to be modeled. The method is benchmarked against eight different classic models in the literature. Based on the findings in this study, the following conclusions may be drawn:

(a) The predictions of classic models for the stress tensor including Smagorinsky, scale similarity, gradient, and models of the mixed kind, vary substantially and are sensitive to variations in filter width.

(b) The standard regularization procedure for evaluating the models' dynamic parameters by averaging in homogeneous directions is inadequate and problematic.

(c) The static and dynamic versions of the Smagorinsky model are not recommended for application to turbulent and reacting flows.

(d) Iterative deconvolution is a robust and accurate modeling framework for all six components of the stress tensor. The method is also the least sensitive to variations in filter width.

(e) The computational cost for some popular classic models is of the same order as for the deconvolution-based model, making the application of the method viable in actual LES.

Deconvolution-based methods can be an attractive alternative for modeling a wide range of unclosed terms, as they are not tied to a specific flow regime or flow variable. Even though the evaluation in this study has been conducted *a priori*, previous successful implementations of approximate deconvolution methods in nonreacting [29,30] as well as reacting LES [31,32] are indicative of the potential of this modeling approach. Further important points regarding this method, which are part of future work, include the effects of filter type, and of discrete filter operator on the predictive ability of the model. With regard to implementation, significant improvements can be obtained, e.g., by exploiting symmetry properties in the case of symmetric filters, and by parallelization on hybrid computer architectures.

[1] M. Klein, C. Kasten, Y. Gao, and N. Chakraborty, *A priori* direct numerical simulation assessment of sub-grid scale stress tensor closures for turbulent premixed combustion, Comput. Fluids **122**, 1 (2015).

[2] J. Smagorinsky, General circulation experiments with the primitive equations, Mon. Weather Rev. **91**, 99 (1963).

[3] R. Fjortof, On the changes in the spectral distribution of kinetic energy for two-dimensional non-divergent flow, Svenska Geophysiska Foreningen, Tellus **5**, 225 (1953).

[4] U. Piomelli, W. H. Cabot, P. Moin, and S. Lee, Sub-grid scale backscatter in turbulent and transitional flows, Phys. Fluids **3**, 1766 (1991).

[5] J. A. Domaradzki, W. Liu, and M. E. Brachet, An analysis of subgrid-scale interactions in numerically simulated isotropic turbulence, Phys. Fluids **5**, 1747 (1993).

[6] R. M. Kerr, J. A. Domaradzki, and G. Barbier, Small-scale properties of nonlinear interactions and subgrid-scale energy transfer in isotropic turbulence, Phys. Fluids **8**, 197 (1996).

[7] B. Tao, J. Katz, and C. Meneveau, Geometry and scale relationships in high Reynolds number turbulence determined from three-dimensional holographic velocimetry, Phys. Fluids **12**, 941 (2000).

[8] B. Tao, J. Katz, and C. Meneveau, Statistical geometry of subgrid-scale stresses determined from holographic velocimetry measurements, J. Fluid Mech. **457**, 35 (2002).

[9] D. K. Lilly, On the application of the eddy viscosity concept in the interial sub-range of turbulence, Report No. 281, National Center for Atmospheric Research (NCAR), 1966.

[10] J. W. Deardoff, A numerical study of three-dimensional turbulent channel flow at large Reynolds numbers, J. Fluid Mech. **41**, 453 (1970).

[11] P. J. Mason and N. S. Callen, On the magnitude of the subgrid-scale eddy coefficient in large-eddy simulations of turbulent channel flow, J. Fluid Mech. **162**, 439 (1986).

[12] M. Germano, U. Piomelli, P. Moin, and W. H. Cabot, A dynamic sub-grid scale eddy viscosity model, Phys. Fluids **3**, 1760 (1991).

[13] P. Moin, K. Squires, W. Cabot, and S. Lee, A dynamic sub-grid scale model for compressible turbulence and scalar transport, Phys. Fluids A **3**, 2746 (1991).

[14] C. Meneveau, T. S. Lund, and W. H. Cabot, A Lagrangian dynamic subgrid-scale model of turbulence, J. Fluid Mech. **319**, 353 (1996).

[15] M. V. Salvetti, *A priori* tests of a new dynamic sub-grid scale model for finite difference large eddy simulations, Phys. Fluids **7**, 2831 (1994).

[16] A. Leonard, Energy cascade in large eddy simulations of turbulent fluid flows, Adv. Geophys. **18**, 237 (1975).
[17] R. A. Clark, Evaluation of sub-grid scalar models using an accurately simulated turbulent flow, J. Fluid Mech. **91**, 1 (1979).
[18] B. Vreman, B. Geurts, and H. Kuerten, Large eddy simulation of the temporal mixing layer using the Clark model, Theor. Comput. Fluid Dyn. **8**, 309 (1996).
[19] J. Bardina, J. H. Ferziger, and W. C. Reynolds, Improved turbulence models based on large eddy simulation of homogeneous, incompressible, turbulent flows, Technical Report No. TF-19, Department of Mechanical Engineering, Stanford University, 1983.
[20] B. Vreman, B. Geurts, and H. Kuerten, Large-eddy simulation of the temporal mixing layer, J. Fluid Mech. **339**, 357 (1997).
[21] F. Nicoud and F. Ducros, Sub-grid scale stress modeling based on the square of the velocity gradient tensor, Flow, Turbul. Combust. **62**, 183 (1999).
[22] C. Meneveau and J. Katz, Scale invariance and turbulence models for large-eddy simulation, Annu. Rev. Fluid Mech. **32**, 1 (2000).
[23] P. Pfandler, F. Beyrau, F. Dinkelacker, and A. Leipertz, A prior testing of an eddy viscosity model for the density-weighted sub-grid scale stress tensor in turbulent premixed flames, Exp. Fluids **49**, 839 (2010).
[24] K. N. C Bray, P. A. Libby, G. Masuya, and J. B. Moss, Turbulence production in premixed turbulent flames, Combust. Sci. Technol. **25**, 127 (1981).
[25] J. Chomiak and J. Nisbet, Modeling variable density effects in turbulent flames—Some basic considerations, Combust. Flame **102**, 371 (1995).
[26] M. Schoepplein, J. Weatheritt, R. Sandberg, M. Talei, and M. Klein, Application of an evolutionary algorithm to LES modeling of turbulent transport in premixed flames, J. Comput. Phys. **374**, 1166 (2018).
[27] B. G. Geurts, Inverse modeling for large eddy simulation, Phys. Fluids **9**, 3585 (1997).
[28] J. A. Domaradzki and E. M. Saiki, A subgrid-scale model based on the estimation of unresolved scales of turbulence, Phys. Fluids **9**, 2148 (1997).
[29] S. Stolz and N. Adams, An approximate deconvolution procedure for large-eddy simulation, Phys. Fluids **11**, 1699 (1999).
[30] S. Stolz and N. Adams, An approximate deconvolution model for large eddy simulation with application to incompressible wall-bounded flows, Phys. Fluids **13**, 997 (2001).
[31] J. Mathew, Large eddy simulation of a premixed flame with approximate deconvolution modeling, Proc. Combust. Inst. **29**, 1995 (2002).
[32] P. Domingo and L. Vervisch, Large eddy simulation of premixed turbulent combustion using approximate deconvolution and explicit flame filtering, Proc. Combust. Inst. **35**, 1349 (2015).
[33] P. Domingo and L. Vervisch, DNS and approximate deconvolution as a tool to analyze one-dimensional filtered flame sub-grid scale modeling, Combust. Flame **177**, 109 (2017).
[34] C. Mehl and B. Fiorina, Evaluation of deconvolution modeling applied to numerical combustion, Combust. Theory Modell. **22**, 38 (2017).
[35] Q. Wang and M. Ihme, Regularized deconvolution method for turbulent combustion modeling, Combust. Flame **176**, 125 (2017).
[36] Z. M. Nikolaou and L. Vervisch, *A priori* assessment of an iterative deconvolution method for LES sub-grid scale variance modeling, Flow Turb. Combust. **101**, 33 (2018).
[37] Z. M. Nikolaou and L. Vervisch, Assessment of deconvolution-based flamelet methods for progress variable rate modeling, Aeron. Aero. Open Access J. **2**, 274 (2018).
[38] Z. M. Nikolaou and N. Swaminathan, Evaluation of a reduced mechanism for turbulent premixed combustion, Combust. Flame **161**, 3085 (2014).
[39] Z. M. Nikolaou and N. Swaminathan, Direct numerical simulation of complex fuel combustion with detailed chemistry: Physical insight and mean reaction rate modeling, Combust. Sci. Technol. **187**, 1759 (2015).
[40] Z. M. Nikolaou, L. Vervisch, and R. S. Cant, Scalar flux modeling in turbulent flames using iterative deconvolution, Phys. Rev. Fluids **3**, 043201 (2018).

[41] I. A. Mullaa, A. Dowlut, T. Hussain, Z. M. Nikolaou, S. R. Chakravarthy, N. Swaminathan, and R. Balachandran, Heat release rate estimation in laminar premixed flames using laser-induced fluorescence of CH_2O and H atom. Combust. Flame **165**, 373 (2016).

[42] D. Drikakis and W. Rider, *High-Resolution Methods for Incompressible and Low Speed Flows* (Springer-Verlag, Berlin, 2005).

[43] N. A. Adams and S. Hickel, Implicit large-eddy simulation: Theory and application, *in Advances in Turbulence XII*, Springer Proceedings in Physics Vol. 132, edited by B. Ekchardt (Springer, Berlin/Heidelberg, 2009).

[44] A. Aspden, N. Nikiforakis, S. Dalziel, and J. B. Bell, Analysis of implicit LES methods, Commun. Appl. Math Comput. Sci. **3**, 103 (2008).

[45] D. Drikakis, M. Hahn, A. Mosedale, and B. Thornber, Large eddy simulation using high resolution and high-order methods, Philos. Trans. R. Soc. A **367**, 2985 (2009).

[46] J. R. Bull and A. Jameson, Explicit filtering and exact reconstruction of the sub-filter stresses in large eddy simulation, J. Comput. Phys. **306**, 117 (2016).

[47] G. Lodato and J.-B. Chapelier, A spectral-element dynamic model for the large-eddy simulation of turbulent flows, J. Comput. Phys. **321**, 279 (2016).

[48] Y. Minamoto, N. Fukushima, M. Tanahashi, T. Miyauchi, and T. Dunstan, Effect of flow geometry on turbulence-scalar interaction in premixed flames, Phys. Fluids **23**, 125107 (2011).

[49] E. Gutheil, G. Balakrishnan, and F. A. Williams, Structure and extinction of hydrogen-air diffusion flames, in *Lecture Notes in Physics: Reduced Kinetic Mechanisms for Applications in Combustion Systems*, edited by N. Peters and B. Rogg (Springer-Verlag, New York, 1993), pp. 177–195.

[50] R. J. Kee, G. Dixon-Lewis, J. Warnatz, M. E. Coltrin, and J. A. Miller, A Fortran computer code package for the evaluation of gas-phase multicomponent transport properties, Report No. SAND86-8246, Sandia National Laboratories, Livermore, CA, 1986.

[51] R. J. Kee, F. M. Rupley, and J. A. Miller, Chemkin-II: A Fortran chemical kinetics package for the analysis of gas phase chemical kinetics, Report No. SAND89-8009B, Sandia National Laboratories, Livermore, CA, 1989.

[52] A. G. Kravchenko and P. Moin, Numerical studies of flow over a circular cylinder at $\mathrm{Re}_D = 3900$, Phys. Fluids **12**, 403 (2000).

[53] C. H. K. Williamson, Vortex dynamics in the cylinder wake, Annu. Rev. Fluid Mech. **28**, 477 (1996).

[54] A. Prasad and C. H. K. Williamson, The instability of the shear layer separating from a bluff body, J. Fluid Mech. **333**, 375 (1997).

[55] A. Prasad and C. H. K. Williamson, The instability of the separated shear layer from a bluff body, Phys. Fluids **8**, 1347 (1996).

[56] B. W. Anderson and J. A. Domaradzki, A subgrid-scale model for large-eddy simulation based on the physics of interscale energy transfer in turbulence, Phys. Fluids **24**, 065104 (2012).

[57] G. Erlebacher, M. Y. Hussaini, C. G. Speziale, and T. A. Zang, Toward the large-eddy simulation of compressible turbulent flows, J. Fluid Mech. **238**, 155 (1992).

[58] A. Yoshizawa, Statistical theory for compressible turbulent shear flows, with the application to sub-grid modeling, Phys. Fluids **29**, 2152 (1986).

[59] D. K. Lilly, A proposed modification of the Germano subgrid-scale closure method, Phys. Fluids **4**, 633 (1992).

[60] Y. Zhang, R. L. Street, and J. R. Koseff, A dynamic mixed subgrid-scale model and its application to turbulent recirculating flows, Phys. Fluids **5**, 3186 (1993).

[61] G. Lodato, L. Vervisch, and P. Domingo, A compressible wall-adapting similarity mixed model for large-eddy simulation of the impinging round jet, Phys. Fluids **21**, 035102 (2009).

[62] P. Schlatter, S. Stolz, and L. Kleiser, LES of transitional flows using the approximate deconvolution model, Int. J. Heat Fluid Flow **25**, 549 (2004).

[63] A. A. Dunca, Estimates of the discrete Van Cittert deconvolution error in approximate deconvolution models of turbulence in bounded domains, Appl. Numer. Math. **134**, 1 (2018).

[64] L. Y. M. Gicquel, G. Staffelbach, and T. Poinsot, Large eddy simulations of gaseous flames in gas turbine combustion chambers, Prog. Energy Combust. Sci. **38**, 782 (2012).